

3D hydrodynamics simulations of a $3 M_{\odot}$ core-helium burning star

Simon Blouin^{1,†,*}, Falk Herwig^{1,†}, Huaqing Mao^{2,†}, Pavel Denissenkov^{1,†}, and Paul R. Woodward^{2,†}

¹*Department of Physics and Astronomy, University of Victoria, Victoria, BC V8W 2Y2, Canada*

²*LCSE and Department of Astronomy, University of Minnesota, Minneapolis, MN 55455, USA*

[†]*Joint Institute for Nuclear Astrophysics – Center for the Evolution of the Elements (JINA–CEE)*

Submitted to MNRAS on 2023-08-17

ABSTRACT

The inner structure of core-helium burning (CHeB) stars remains uncertain due to the yet unknown nature of mixing at the boundary of their cores. Large convective cores beyond a bare Schwarzschild model are favoured both from theoretical arguments and from asteroseismological constraints. However, the exact nature of this extra mixing, and in particular the possible presence of semiconvective layers, is still debated. In this work, we approach this problem through a new avenue by performing the first full-sphere 3D hydrodynamics simulations of the interiors of CHeB stars. We use the PPMstar explicit gas dynamics code to simulate the inner $0.45 M_{\odot}$ of a $3 M_{\odot}$ CHeB star. Simulations are performed using different Cartesian grid resolutions (768^3 , 1152^3 and 1728^3) and heating rates. We use two different initial states, one based on MESA’s predictive mixing scheme (which yields a large overshoot region) and one based on the convective premixing approach (which exhibits a semiconvective interface). The general behaviour of the flow in the convective core and in the stable envelope (where internal gravity waves are observed) is consistent with our recent simulations of core convection in massive main-sequence stars, and so are the various scaling relations. The semiconvective layers are dominated by strong internal gravity waves that do not produce measurable species mixing, but overshooting motions from the convective core gradually homogenize the semiconvective interface. This process can possibly completely erase the semiconvective layers, which would imply that CHeB stars do not harbour a semiconvection zone.

Key words: convection – hydrodynamics – methods: numerical – stars: horizontal branch – stars: interiors

1 INTRODUCTION

Core helium burning (CHeB) stars are characterized by a central convective He-burning core surrounded by a convectively stable He-rich envelope. Observationally, CHeB stars are known as red clump stars, secondary clump stars, RR-Lyrae, horizontal branch stars, or subdwarfs B. These various classes of CHeB stars descend from different evolutionary pathways, but they all have a He-fusing core where the triple- α reaction produces carbon and $^{12}\text{C}(\alpha, \gamma)^{16}\text{O}$ makes oxygen.

In low- and intermediate-mass stars, the treatment of convective boundary mixing (CBM) at the edge of the He-fusing core is particularly challenging for 1D stellar evolution (e.g., see the review by Salaris & Cassisi 2017). The generation of C and O inside the convective core enhances its opacity κ , and the radiative gradient,

$$\nabla_{\text{rad}} = \frac{3}{16\pi acG} \frac{\kappa LP}{mT^4}, \quad (1)$$

increases in the convection zone. In Equation (1), a is the radiation constant, c is the speed of light, G is the gravitational constant, L is the luminosity, P is the pressure, m is the mass enclosed within the radius at which ∇_{rad} is calculated, and T is the temperature. This ∇_{rad} increase leads to the formation of a discontinuity, such that $\nabla_{\text{rad}} > \nabla_{\text{ad}}$ just inside the core and $\nabla_{\text{rad}} = \nabla_{\text{ad}}$ just outside (blue solid line in Figure 1), where ∇_{ad} is the adiabatic temperature gradient. By definition, the convective boundary is located at the radius

where radiation carries out all the energy. Within the mixing length theory (MLT) framework used in many 1D stellar evolution calculations, this condition is satisfied where the Schwarzschild criterion $\nabla_{\text{rad}} = \nabla_{\text{ad}}$ is met (Biermann 1932). It is of course well established that convective penetration can significantly shift the location of the convective boundary with respect to the Schwarzschild boundary (for recent multi-dimensional simulations demonstrating this point, see Käpylä 2019; Anders et al. 2022a; Androssy et al. 2023; Baraffe et al. 2023; Blouin et al. 2023b; Mao et al. 2023), but it is instructive in what follows to consider the consequences of applying the standard Schwarzschild criterion to the He-burning core.

Within this framework, $\nabla_{\text{rad}} = \nabla_{\text{ad}}$ must be satisfied on the *convective side* of the boundary, since otherwise the convective flux cannot be zero (Gabriel et al. 2014). In CHeB stars, we encounter a situation where $\nabla_{\text{rad}} = \nabla_{\text{ad}}$ on the radiative side of the ∇_{rad} discontinuity, but where $\nabla_{\text{rad}} > \nabla_{\text{ad}}$ on the convective side. Therefore, the convective flux is not zero at that location, and this cannot be the convective boundary. This conclusion can also be reached by realizing that the Schwarzschild boundary is in an unstable equilibrium (Schwarzschild & Härm 1969; Castellani et al. 1971a). If the layer just above the convection zone is mixed with the core, its opacity increases due to the inflow of opaque C/O-rich material, ∇_{rad} surpasses the adiabatic gradient, and the convective core grows. Mixing of the layer immediately above the core is inevitable: any amount of convective overshooting can accomplish that, and even atomic diffusion alone could be sufficient (Michaud et al. 2007).

To find a stable boundary, the convective core must be extended

* E-mail: sblouin@uvic.ca

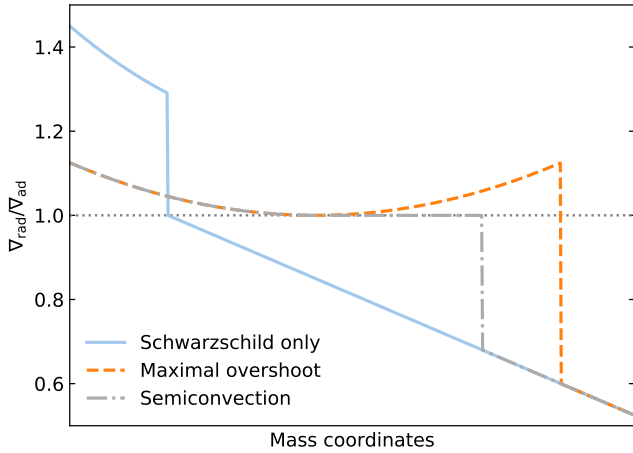


Figure 1. Qualitative representation of the radiative gradient profiles described in Section 1.

until $\nabla_{\text{rad}} = \nabla_{\text{ad}}$ on the convective side of the Schwarzschild boundary, but this leads to further complications. Given the behaviour of the opacity and the thermodynamic structure of CHeB stars, extending the core leads to the formation of a local minimum in ∇_{rad} within the convective region. Eventually, this local minimum in ∇_{rad} reaches ∇_{ad} , effectively splitting the convective region in two. What does that mean for mixing in the star? Full mixing of the gap now separating the convective core from the convective shell above is problematic as it would imply the formation of a region with $\nabla_{\text{rad}} < \nabla_{\text{ad}}$ at the local minimum, in contradiction with the assumption of full mixing.

Two families of solutions have been proposed to solve this problem within the 1D MLT framework. The first consists of the formation of a partially mixed (or semiconvective) region between the ∇_{rad} local minimum and the radiative envelope (Schwarzschild & Härm 1969; Paczyński 1970; Castellani et al. 1971b). In this scenario, an extended semiconvective region where $\nabla_{\text{rad}} = \nabla_{\text{ad}}$ separates the convective core from the stable layers (grey dash-dotted line in Figure 1). This CBM prescription has been implemented in many stellar evolution codes (e.g., Dorman & Rood 1993; Cassisi et al. 2003; Constantino et al. 2015), including in MESA through the convective premixing scheme (CPM, Paxton et al. 2019; Ostrowski et al. 2021). Another solution consists of artificially halting the growth of the convective core before the splitting occurs. This is known as maximal overshoot (Constantino et al. 2015; Denissenkov et al. 2017; Li et al. 2018, in the case where the growth is stopped just before the point where splitting would take place) or predictive mixing (PM, Paxton et al. 2018; Ostrowski et al. 2021). In this scenario, there is no partially mixed zone and, problematically, ∇_{rad} remains greater than ∇_{ad} on the inner side of the convective boundary (orange dashed line in Figure 1).

It is unclear which of these two approaches should be preferred in 1D stellar evolution calculations, but some insights can be gained from observational constraints. Asteroseismological studies of various flavours of CHeB stars have clearly established that a bare Schwarzschild core (i.e., no extra CBM, as in the blue solid line of Figure 1) can be ruled out. A more extended convective core is definitely required to reproduce the observed pulsation periods (Van Grootel et al. 2010a,b; Charpinet et al. 2011, 2019b; Montalbán et al. 2013; Bossini et al. 2015; Constantino et al. 2015; Uzundag et al. 2021). A similar conclusion is reached via cluster star counts, which are used to infer the lifetimes of horizontal branch stars (Constantino

et al. 2016). But beyond this finding, CHeB asteroseismological constraints do not yet offer a clear answer regarding which CBM scheme should be adopted. Constantino et al. (2015, 2016) conclude that both the maximal overshoot and semiconvective prescriptions can be compatible with observations of horizontal branch stars. Similarly, for subdwarfs B, Uzundag et al. (2021) find that both the PM (or maximal overshoot) and CPM (or semiconvective) schemes implemented in MESA produce core masses that are in better agreement with the observations than bare Schwarzschild models (although even then the core sizes remain below the seismically derived values).

Another promising observational window is white dwarf asteroseismology. The composition profiles of white dwarf C-O cores bear the imprint of the CHeB phase (Straniero et al. 2003; Salaris et al. 2010; Chidester et al. 2023): empirically derived white dwarf internal stratifications provide valuable constraints on CHeB CBM. Recently, Giammichele et al. (2018, 2022) have mapped the core compositions of a handful of white dwarfs using flexible internal profiles that make no explicit assumption on the nature of CBM in pre-white dwarf evolutionary phases (see also Charpinet et al. 2019a). Standard evolution models fail to reproduce these seismically derived stratifications (De Gerónimo et al. 2019), which contain a large O-rich central region. Giammichele et al. (2022) suggest that this situation may be due to the artificial inhibition of breathing pulses in CHeB evolution models. Towards the end of the CHeB phase, when the convective core contains less than $\approx 10\%$ He, the production of O via $^{12}\text{C}(\alpha, \gamma)^{16}\text{O}$ leads to a rapid increase of the opacity. The ingestion of a small amount of fresh He into the core then triggers a sharp increase of ∇_{rad} and a sudden growth of the core, which subsides on a short timescale as the star readjusts its structure. These events are known as breathing pulses (Sweigart & Demarque 1973; Castellani et al. 1985). Breathing pulses are often considered to be numerical artefacts and, accordingly, they are usually suppressed from evolutionary calculations (e.g., Cassisi et al. 2001, 2003; Spruit 2015; Constantino et al. 2017; Paxton et al. 2018). Giammichele et al. (2022) argue that breathing pulses may be real after all, although this view would have to be reconciled with the fact that cluster star counts favour models without breathing pulses (which have shorter horizontal branch lifetimes, Caputo et al. 1989; Cassisi et al. 2001, 2003; Constantino et al. 2017).

Better understanding CBM in CHeB stars would have important ramifications beyond CHeB stars. In particular, extra mixing during the CHeB phase ultimately leads to the formation of white dwarfs with more O-rich cores, and the exact O abundance profile of white dwarfs is a key determinant of their cooling rates. Not only does it determine the total thermal energy content of the star (Fontaine et al. 2001), but it also controls how much energy is released by fractionation processes during core crystallization (Segretain et al. 1994; Montgomery et al. 1999; Salaris et al. 1997, 2000; Althaus et al. 2012; Blouin et al. 2020, 2021). Due to current uncertainties related to CBM during the CHeB phase, the O abundance profile of white dwarfs remains poorly constrained (Salaris et al. 2010, 2022), and this injects systematic errors in the white dwarf cooling models (Renedo et al. 2010; Bédard et al. 2020; Salaris et al. 2022; Bauer 2023) used in diverse age-dating applications (Hansen et al. 2013; Fantin et al. 2019; Boylan-Kolchin & Weisz 2021; Kaiser et al. 2021; Cimatti & Moresco 2023). For the oldest white dwarfs in the Milky Way, CHeB CBM uncertainties result in errors of the order of a Gyr on inferred ages.

In this work, we use full-sphere 3D stellar hydrodynamics simulations of the interiors of CHeB stars to confront the CHeB CBM problem from a yet unexplored angle. Our simulations, performed with the PPMstar explicit gas dynamics code, follow for dozens

of convective turnover timescales the 3D hydrodynamics response of the gas to a given CHeB structure. We study the behaviour of the flow for the two commonly used 1D CBM prescriptions, MESA’s PM and CPM schemes. We describe these MESA models in Section 2, where we also explain how our PPMstar simulations are initialized. The general properties of the 3D simulations (flow morphology, convergence with respect to grid resolution, scaling relations) are explored in Section 3. In Section 4, we study mixing and entrainment in our simulations and discuss the implications of our findings in the context of the CHeB CBM problem. Finally, we conclude in Section 5.

2 METHODS

In this section, we first describe the calculations we have performed with the MESA code to initialize our PPMstar simulations. In Section 2.2 we then explain how the MESA models were mapped into our 3D simulations. Finally, we detail the PPMstar simulations themselves in Section 2.3.

2.1 MESA evolution sequences

We use MESA version 12115 (Paxton et al. 2011, 2013, 2015, 2018, 2019) to generate our CHeB setups. We calculated the evolution of a $3 M_{\odot}$ star from the pre-main sequence to the end of the CHeB phase. We chose an initial He mass fraction $Y = 0.27$ and an initial metallicity $[\text{Fe}/\text{H}] = -0.3$ using the Asplund et al. (2009) abundance ratios. The mixing length is fixed to $\ell = 2H_P$ (where H_P is the local pressure scale height), and an overshoot parameter $f_{\text{ov}} = 0.015$ was assumed for the pre-CHeB evolution. When the beginning of the CHeB phase is reached, we separate the calculation into two distinct sequences: one using the PM scheme (Paxton et al. 2018) and one using the CPM scheme (Paxton et al. 2019). For the PM calculation, we use a value of 0.005 for the `predictive_superad_thresh` parameter that controls the maximum extent of the convective core by enforcing a minimal value to $\nabla_{\text{rad}}/\nabla_{\text{ad}} - 1$ in the mixed region. In the case of the CPM calculation, a very high spatial and temporal resolution is required to produce a smooth stratification at the core boundary: we use `mesh_delta_coeff=0.2` and `max_years_for_timestep=10000`.

Figure 2 shows the Kippenhahn diagram of our PM MESA model during a portion of the CHeB phase. The convective core is in grey at the bottom and the nuclear burning regions are in dark blue (He burning at the center and H burning above in the stable envelope). The vertical dashed line indicates the particular model that we have elected to use as an initial state for our 3D simulations. It corresponds to a point where the central He mass fraction has reached $Y_c = 0.31$ and the He-burning luminosity is $L_{\star, \text{He}} = 62.5 L_{\odot}$.¹ We have used the same value of Y_c to select the MESA model to use in the CPM case. Note that the vertical extent of the dashed line in Figure 2 represents the total mass included in our PPMstar simulations ($0 < R < 40$ Mm in terms of radius): only a small portion of the envelope is considered and the H-burning shell is avoided. This is well justified here as anything that occurs above 40 Mm is largely irrelevant to our study of mixing processes close to the convective core boundary, and extending the setup further out would decrease the grid resolution in the region of interest.

¹ For the sake of brevity in our notation, we will denote the He-burning luminosity as L_{\star} in what follows.

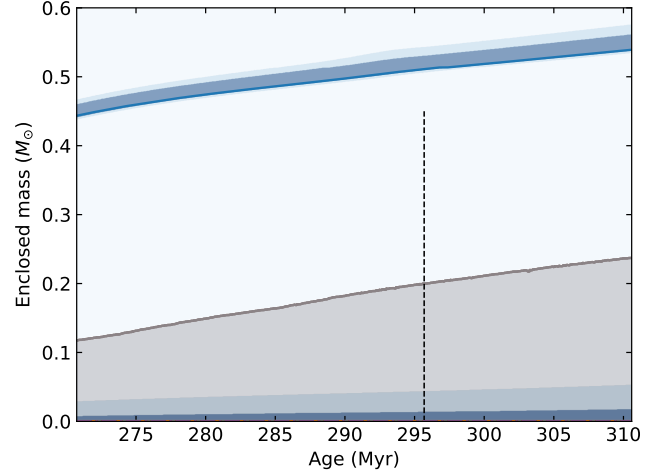


Figure 2. Kippenhahn diagram of the CHeB phase as calculated in our PM MESA run. The dark blue regions show where nuclear burning takes place (He burning at the center and H burning further out), and the grey region shows the extent of the convective core. The dashed vertical line marks the model used for our 3D PPMstar calculations; its vertical extent corresponds to the total mass included in the simulations.

2.2 MESA→PPMstar mapping

As in our recent PPMstar simulations of various types of stars (Blouin et al. 2023a,b; Herwig et al. 2023; Mao et al. 2023), the initial 3D state is reconstructed from the MESA entropy (S) and mean molecular weight (μ) profiles. The PPMstar base state is calculated using these profiles and enforcing hydrostatic equilibrium. This integration is performed using PPMstar’s equation of state, which guarantees that our initial state is precisely in hydrostatic equilibrium. Note that small-scale noise was filtered out from the raw MESA S and μ profiles to avoid injecting spurious small-scale structures into the 3D base state. In addition, we smoothed the S and μ profiles at the outer edge of the semiconvection zone (in the CPM case) and of the convective core (in the PM case) as the CPM and PM schemes each produce unphysical discrete jumps. These transition regions were flattened so that they span at least 10 grid cells in our PPMstar simulations. This procedure is shown in the top panels of Figures 3 and 4.

The equation of state currently implemented in PPMstar includes the pressure contributions from the ideal gas and from the radiation field,

$$P = P_{\text{gas}} + P_{\text{rad}} = \frac{R\rho T}{\mu} + \frac{aT^4}{3}, \quad (2)$$

where R is the ideal gas constant. In the central layers of CHeB stars, additional contributions from electron degeneracy pressure and ion-ion nonideal interactions come into play. As a result there is a $\approx 10\%$ mismatch between the central pressure in our MESA models and that in our PPMstar setups (see third panels of Figures 3 and 4). A difference of that magnitude is not expected to impact the dynamics of the simulations in any meaningful way. Indeed, in our previous work on massive main-sequence stars, we have found the neglect of the radiation pressure term (which accounts for $\approx 20\%$ of the pressure in the $25 M_{\odot}$ star we have studied) to be an excellent approximation (Herwig et al. 2023; Mao et al. 2023). However, we will see in Section 4 that this mismatch complicates the interpretation of the observed migration of the convective/semiconvective boundary over the course of our simulations.

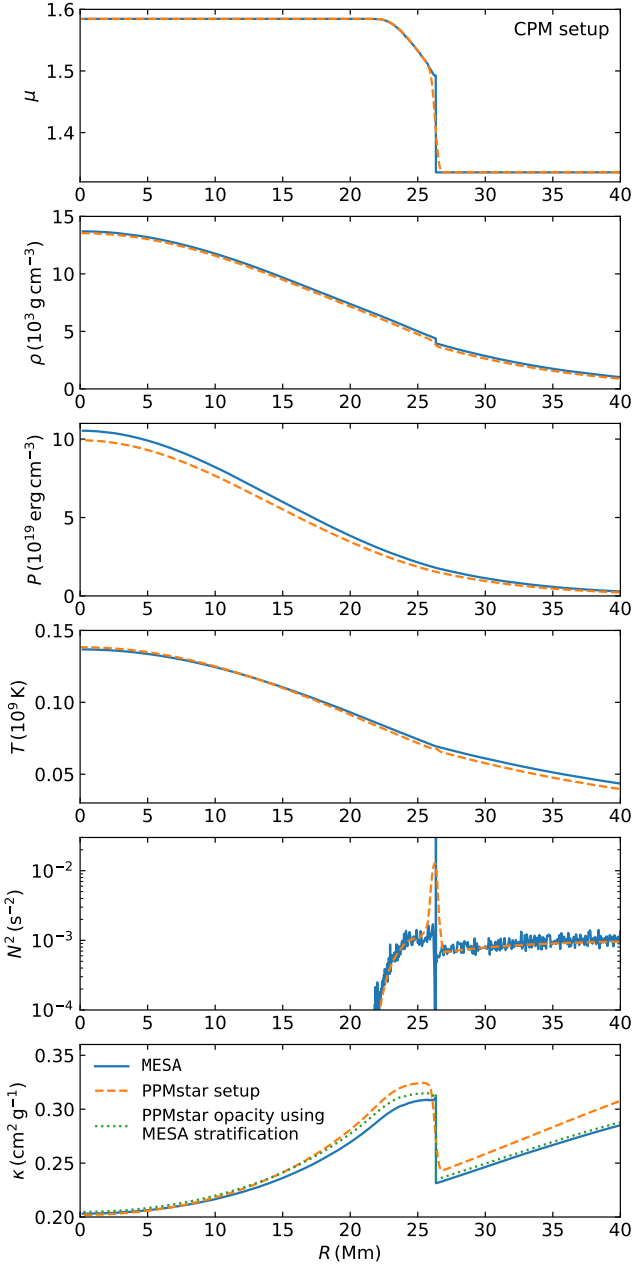


Figure 3. Radial profiles for our CPM setup. The MESA profile (blue solid line) and the base state of our PPMstar simulations (dashed orange line) are shown for each quantity. In the last panel, the dotted green line shows the opacity profile obtained using the MESA stratification and the PPMstar opacity module. The semiconvection zone is the region between $R \approx 22$ and 26 Mm characterized by a shallow μ gradient.

Our PPMstar simulations include radiative diffusion via a radiative flux term in the energy equation (Mao et al. 2023),

$$\mathbf{F}_{\text{rad}} = -\frac{4acT^3}{3\kappa\rho} \nabla T. \quad (3)$$

To model the opacity κ , we use the OPAL tables (Iglesias & Rogers 1996). Since table look-ups would be too inefficient for a highly optimized code like PPMstar, we have built a polynomial expression that reliably approximates the OPAL tables in the limited

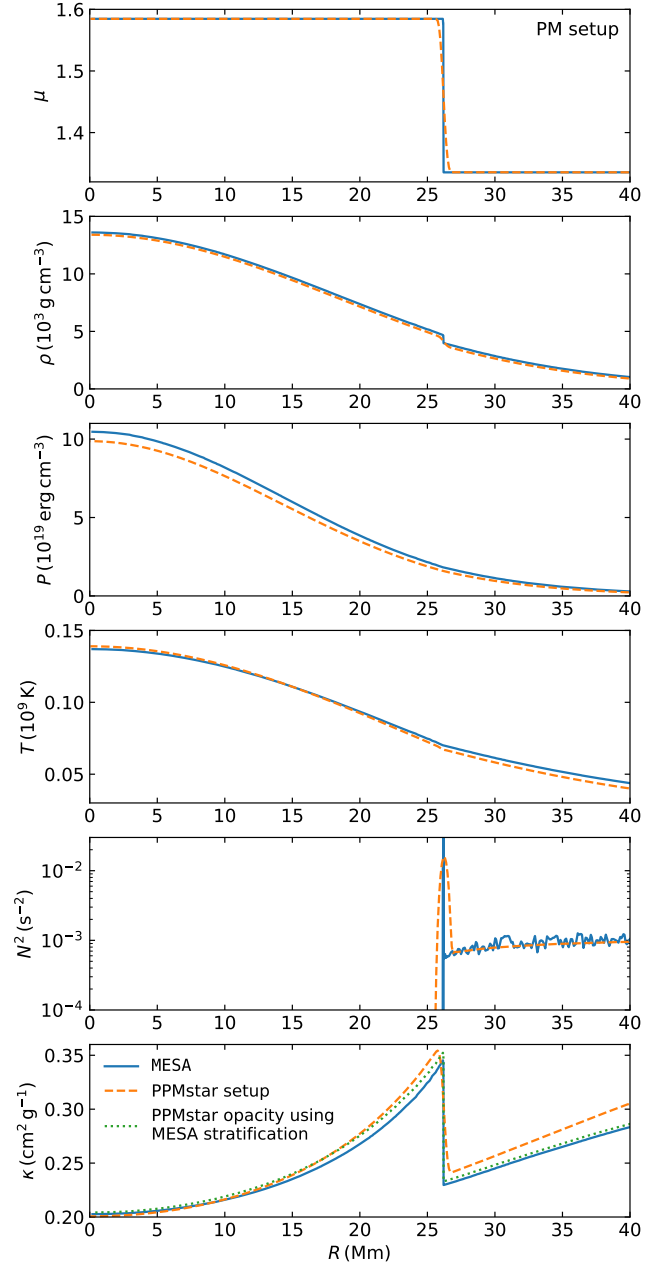


Figure 4. Same as Figure 3 but for our PM setup.

composition–temperature–density space explored in our simulations (Appendix A). As shown in the bottom panels of Figures 3 and 4, this simple prescription reliably captures the dependence of κ on the composition and physical conditions. The green dotted lines obtained with this opacity model closely match the opacities calculated by MESA (blue solid lines). The opacity profile actually used in our simulations (orange dashed lines) departs more significantly from the MESA profiles. This is caused by the differences between the thermodynamic structures of the star in MESA and in PPMstar due to the incomplete equation of state.

Table 1. Summary of simulations used in this work.

Run ID	Setup	Grid	$\log L/L_\star$	# dumps	Duration (h)
W10	CPM	768 ³	6.0	2324	56.3
W11	PM	768 ³	6.0	1958	47.3
W12	CPM	768 ³	5.0	1080	26.1
W13	PM	768 ³	5.0	1227	29.6
W16	CPM	768 ³	4.5	1092	26.4
W17	PM	768 ³	4.5	1266	30.6
W20	CPM	1728 ³	5.0	1318	31.9
W21	PM	1728 ³	5.0	1348	32.6
W22	CPM	1152 ³	5.0	1718	60.6
W23	PM	1152 ³	5.0	1621	61.1
W24	CPM	768 ³	5.5	1097	26.6
W25	PM	768 ³	5.5	1329	32.1
W26	CPM	1152 ³	5.5	1193	48.1
W27	PM	1152 ³	5.5	1215	48.9
W28	CPM	1152 ³	6.0	1196	48.3
W29	PM	1152 ³	6.0	1039	41.8
W30	CPM	1152 ³	4.5	1179	47.6
W31	PM	1152 ³	4.5	1204	48.5
W32	CPM	768 ³	7.0	1706	41.3
W33	PM	768 ³	7.0	1513	36.6

2.3 PPMstar simulations

PPMstar is an explicit gas dynamics code where the conservation equations are solved on a 3D Cartesian grid (Woodward et al. 2015, 2018, 2019; Jones et al. 2017; Andrassy et al. 2020; Herwig et al. 2023). In our simulations, the nuclear energy source from He burning in the core is modelled by a constant volume heating following a Gaussian radial profile that matches the MESA heating profile. Two fluids are included in the calculations: one having the mean molecular weight of the C/O-rich core ($\mu = 1.5845$) and one having the mean molecular weight of the almost pure-He envelope ($\mu = 1.3359$).

All our simulations are performed with heating luminosities that exceed the nominal He burning luminosity L_\star of the star. MLT predicts a convective Mach number smaller than 10^{-4} in the He-burning cores of our $3 M_\odot$ stars. As PPMstar is an explicit gas dynamics code, accurately resolving such slow flows would demand prohibitively small simulation grid cells. To circumvent this problem, we apply a boost factor to L_\star . We will present heating series (i.e., series of simulations that are identical except for their heating boost factors) in Section 3.3 that can be used to extrapolate our results to nominal luminosity. Another benefit of calculating heating series is that deviations from established scaling laws at low luminosities can be used to identify numerical resolution issues. Note that the radiative conductivity,

$$K = \frac{4acT^3}{3\kappa\rho}, \quad (4)$$

is always multiplied by the same boost factor to ensure energy conservation in the star. If more heat is generated in the central layers, then it must be transported more efficiently by radiation. We also perform simulations for three different grid resolutions to assess the numerical convergence of our calculations (Section 3.2). All simulations discussed in this work are listed in Table 1.

The analysis of our simulations relies on three types of outputs (Andrassy et al. 2020; Stephens et al. 2021; Herwig et al. 2023). Every 1000–3000 time steps (depending on the grid resolution), a detailed output (“dump”) is written to disk. Each of these dumps contains spherically averaged profiles, high-precision 3D briquette data (on a grid that is four times smaller in each direction than the

simulation grid), and full-resolution byte-sized data cubes that we use to generate qualitative visualizations of the flow.

As shown in Table 1, each simulation is run for 25–60 h of star time. As we will see in the next section, the rms velocity in the convective core for the $\log L/L_\star = 5$ simulations is of the order of 4 km s^{-1} . This implies a convective turnover timescale of $\sim 2 \times 25 \text{ Mm}/4 \text{ km s}^{-1} \sim 3 \text{ h}$, and our simulations therefore span ~ 10 – 50 convective turnover timescales (depending on the heating rate and total simulation length). This is sufficient to robustly measure the mean properties of the flow. We show in Figure 5 the time evolution of the spherically averaged convective velocity at a radius located $2 H_P$ (15 Mm) inside the convective boundary. We can see that for almost all simulations, a state that is stationary on the convective timescale is reached after just a few turnover timescales (~ 10 h). The initial transient before that time, when the convective flow is still building up, is discarded from our analysis in the rest of this work. Note that some of the low-heating runs at $\log L/L_\star = 4.5$ take more time to reach a stationary state (see W31 in particular); we will ignore these simulations in most of our analysis.

3 GENERAL PROPERTIES OF THE SIMULATIONS

3.1 Velocity renderings

We first investigate the qualitative behaviour of the flow in our simulations. Figures 6 and 7 are center-plane slice renderings of the tangential² (left panels) and radial (right panels) velocity components in our high-resolution 1728³ CPM and PM simulations. The most striking feature of these renderings is the large dipole-like structure that dominates the convective core, a finding that echoes our recent massive and supermassive H-burning core-convection simulations (Herwig et al. 2023; Blouin et al. 2023a). In Figure 6, we can clearly see in bright orange the large plume travelling from the centre and toward the north in the radial velocity rendering. When it hits the convective boundary, this rising plume is split into two diverging flows travelling in the tangential direction, which forms the characteristic horseshoe-like structure in the horizontal velocity rendering. As described in Herwig et al. (2023), these two tangential flows ultimately separate from the boundary due to their opposing pressure gradients when they eventually travel towards one another, thereby forming an inward moving plume. The same general behaviour can be observed in Figure 7 for the PM setup. It takes a few convective turnover timescales for this dipolar circulation pattern to establish itself, but once it does, it remains a persistent characteristic of the flow. Note however that the dipole structure is not fixed: the movies available at <https://www.ppmstar.org> clearly show that its intensity and orientation fluctuate with time.

A comparison of the tangential velocity renderings of Figures 6 and 7 immediately reveals the very different nature of the convective boundary region in both setups. In the PM case, there is a sharp transition between the high convective velocities of the core and the much smaller velocities that characterize the stable envelope (which are barely visible in these renderings). In contrast, in the CPM simulations, the semiconvection zone imprints a region of moderate velocities between the high velocities of the convective core and low velocities of the stable envelope. It is evident from the ring-like structure of the flow in this region that the semiconvection zone is not dominated by turbulent convective motions. This will be investigated in more detail in Section 3.4.

² By tangential we mean in the plane perpendicular to the radial direction.

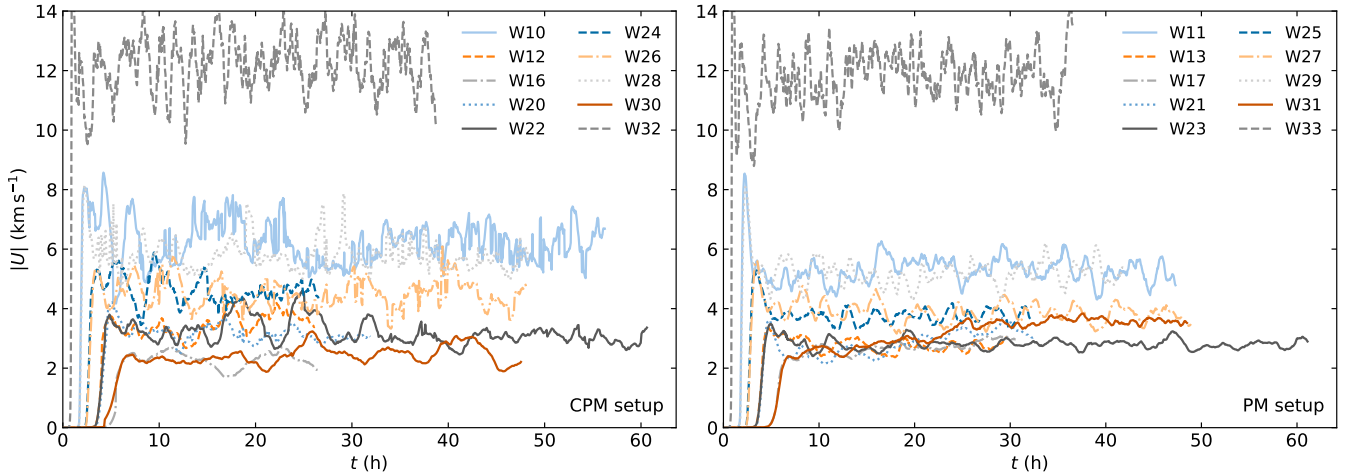


Figure 5. Time evolution of the spherically averaged rms convective velocity $|U|$ at a radius located $2 H_P$ (15 Mm) inside the convective boundary. The left panel shows the runs using the CPM setup and the right panel the PM setup. Most simulations reach a stationary state after a few convective turnover timescales.

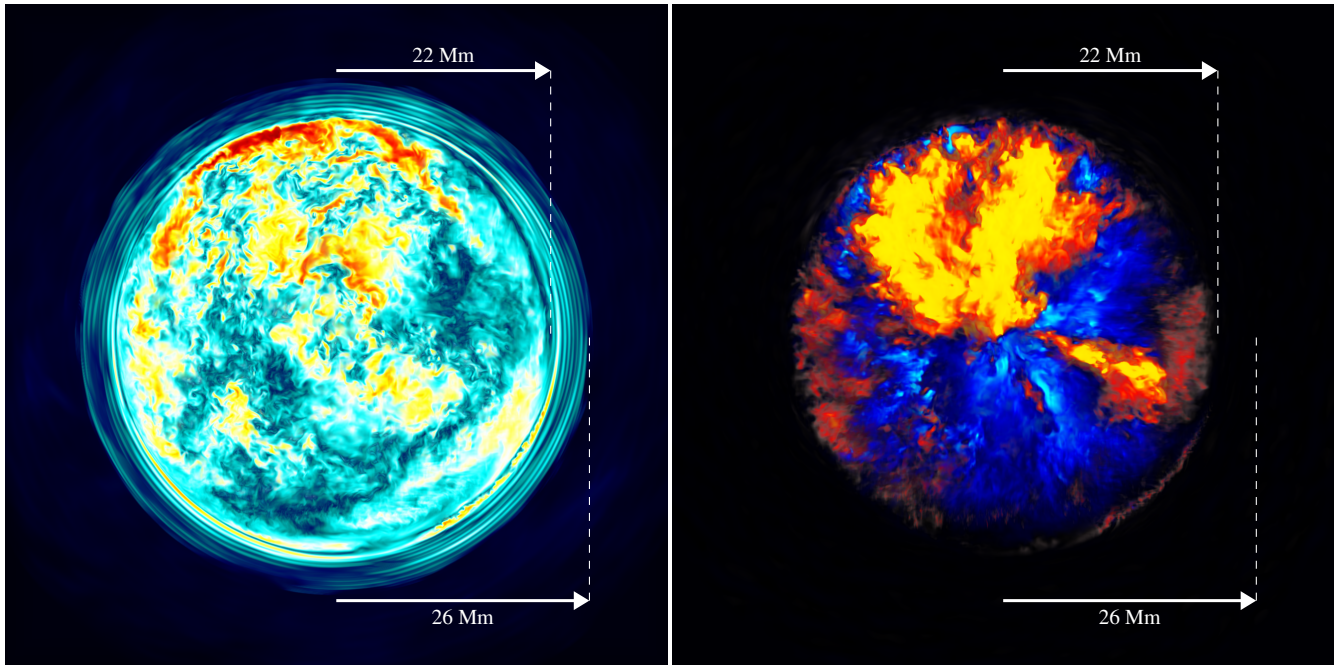


Figure 6. Centre-plane slice rendering of run W20 (CPM setup, 1728^3 grid) at dump 1300 ($t = 31.4$ h). *Left:* magnitude of the tangential velocity component $|U_t|$ (i.e., perpendicular to the radial direction), with dark blue, turquoise, yellow, red, and dark red representing a sequence of increasing velocities. *Right:* radial velocity U_r , with blue colours representing inward-moving flows and red-orange colours outward-moving flows. These renderings were generated to qualitatively visualize the important features of our simulations. The full simulation domain is not shown here: only a $68 \text{ Mm} \times 68 \text{ Mm}$ region is displayed. High-resolution movies are available at <https://www.ppmstar.org>.

3.2 Convergence with respect to the grid resolution

In Figure 8 we compare the spherically averaged velocity profiles of our $\log L/L_\star = 5$ simulations performed using three different grid resolutions. For both setups, our results indicate that the properties of the flow in the convective core and in the boundary region are already well converged with respect to the grid resolution at 1152^3 since there is little difference between the 1152^3 and 1728^3 cases. The situation is less favourable in the envelope. With the CPM setup, there is no sign of convergence of the envelope velocities with respect to the

simulation grid. The situation is better in the case of the PM setup, where the decreasing velocity difference between successive grid refinements suggests that the velocities are approaching convergence.

The slower convergence of the velocities in the envelope compared to the core is at least partially due to the smaller velocities in that region of the star. At the $\log L/L_\star = 5$ heating rate shown in Figure 8, the Mach number in the envelope is only of the order of 10^{-4} , a challenging regime for an explicit gas dynamics code. This also implies that a faster convergence is expected for our simulations with higher heating luminosities, as the flow in the envelope will be

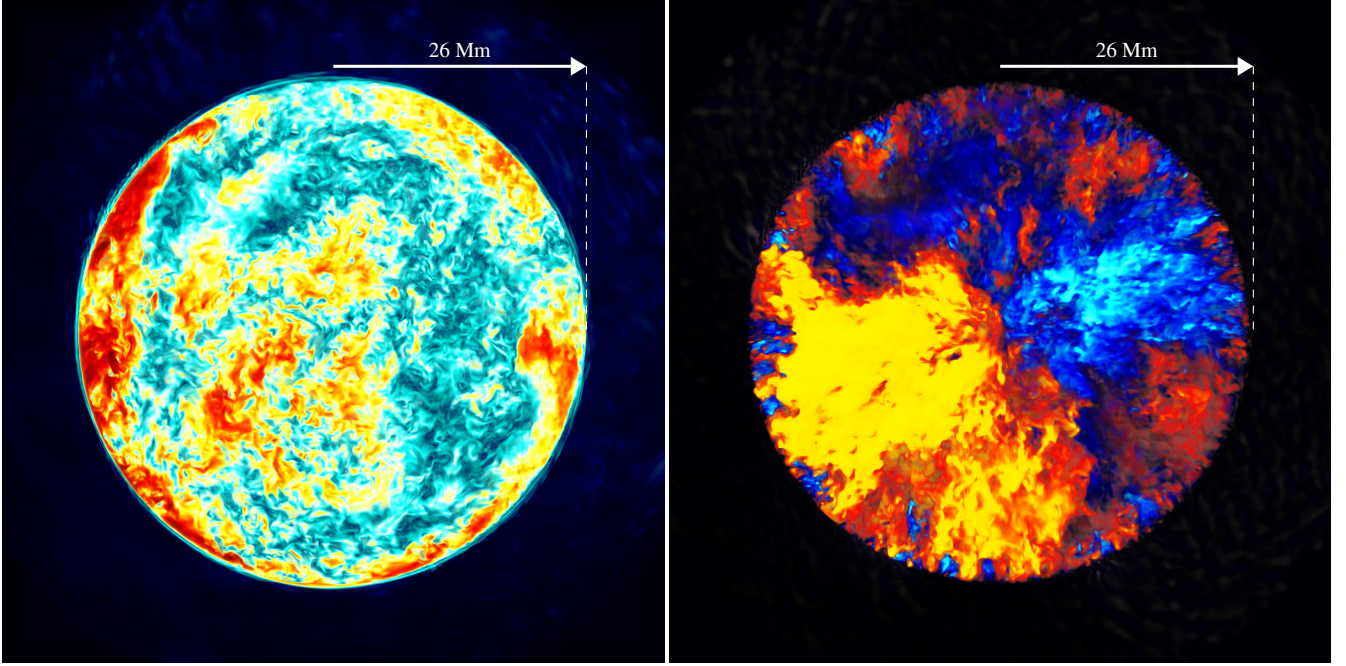


Figure 7. Identical to Figure 6 but for run W21 (PM setup, 1728^3 grid) at dump 1300 ($t = 31.4$ h). The image scale is identical to that of Figure 6.

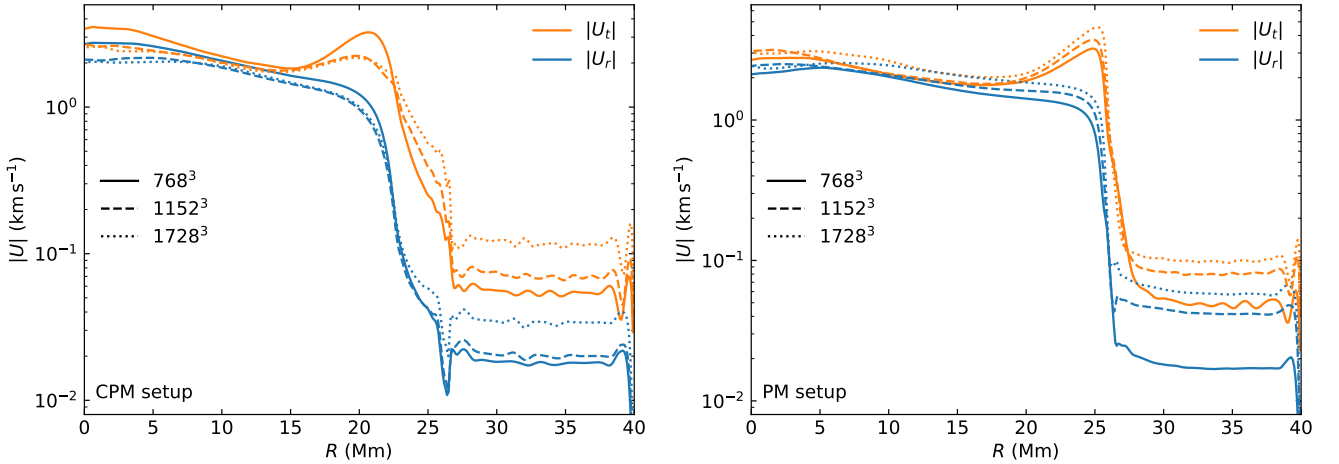


Figure 8. Spherically averaged tangential (orange) and radial (blue) velocity profiles for the CPM (left) and PM (right) setups for different grid resolutions. Simulations W12, W13, W20, W21, W22 and W23 were used to generate this figure ($\log L/L_\star = 5$ heating). The velocity profiles were obtained by averaging over the last 400 dumps of each simulation.

more vigorous (Section 3.3). In any case, this issue is not a major concern in what follows, as the central goal of this work is to study the boundary region where for both setups the velocities converge much faster with respect to the grid resolution.

We have seen that our PM simulations develop a fully convective core separated from the stable He envelope by a well-defined boundary (Figures 7–8). It is unsurprising to find a large fully mixed core with the PM prescription, but it is still interesting to note that we cannot identify any impact on the gas dynamics resulting from the presence of a region in the core where the Schwarzschild criterion is barely satisfied. Indeed, at $R = 21.3$ Mm, $\nabla_{\text{rad}} - \nabla_{\text{ad}}$ reaches its minimum in the convective core of just 0.002, and yet there is no obvious slowdown of the convective motions in that region (right panel of Figure 8). The global dipolar circulation pattern is completely obli-

ous to the presence of this minimum. At least at the heating rates of our simulations, this result confirms that it is consistent to assume full mixing in regions that have $\nabla_{\text{rad}} - \nabla_{\text{ad}} > 0$ by an arbitrarily small margin, as assumed in the maximum overshoot prescription and with MESA’s PM scheme.

3.3 Heating series

As explained in Section 2.3, all our simulations are performed using heating luminosities that far exceed the nominal luminosity of the star. It is therefore important to understand how the properties of the flow scale with respect to the heating rate in order to properly extrapolate to the nominal case. To do so, we show in Figure 9 the rms velocity $|U|$ in the convective core at $R = 15$ Mm as a function

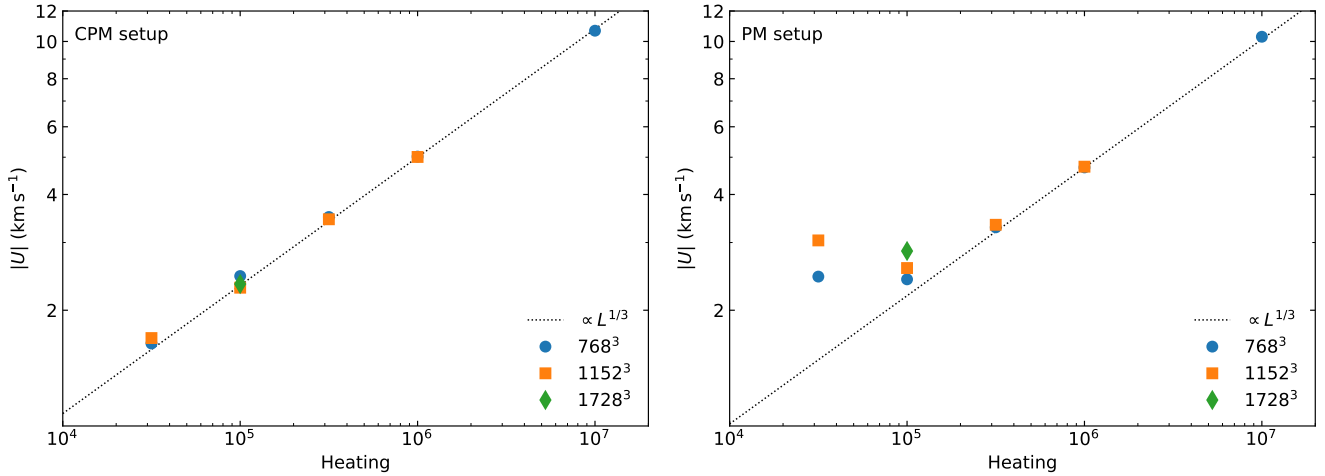


Figure 9. Average velocity in the convective core at $R = 15$ Mm as a function of the heating factor L/L_\star . Results for the CPM setup are shown in the left panel and those for the PM setup are shown in the right panel. The different symbols indicate the grid resolution. For reference, the dotted line shows a $L^{1/3}$ power law. All simulations listed in Table 1 were used to generate this figure. The rms velocities were averaged over the last 15 h of each simulation.

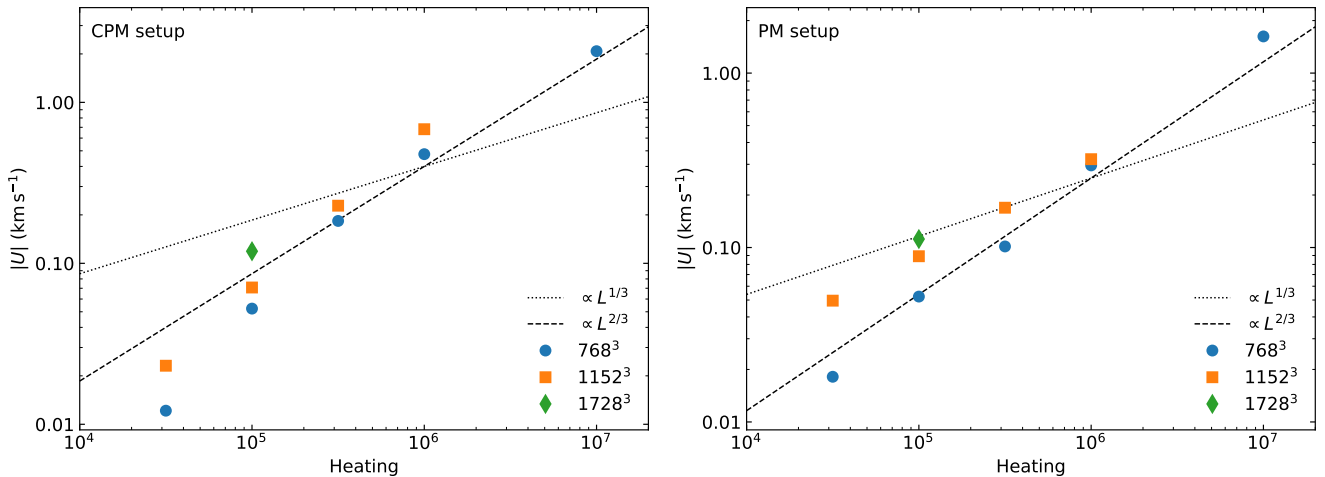


Figure 10. Same as Figure 9, but this time looking at the velocities at $R = 33$ Mm in the stable envelope.

of L/L_\star . For the CPM setup, we precisely recover a $L^{1/3}$ scaling law, as expected based on previous results of 3D hydrodynamics simulations of convection in stars (e.g., Porter & Woodward 2000; Müller et al. 2016; Jones et al. 2017; Baraffe et al. 2021; Herwig et al. 2023). Note also the excellent convergence with respect to the grid resolution: there is virtually no difference between results obtained using a 768^3 , 1152^3 or 1728^3 grid. However, the situation is different for the PM setup. Departures from the $L^{1/3}$ power law appear at $\log L/L_\star \leq 5$, where the $|U|$ values also vary with respect to the grid resolution. Given that the convective velocities are similar for both setups, it is surprising to see this departure from the expected scaling law in the PM setup while the expected behaviour is recovered down to at least $\log L/L_\star = 4.5$ in the CPM case. Nevertheless, the fact that the $L^{1/3}$ power law still applies for $\log L/L_\star \geq 5$ supports the use of this scaling relation to extrapolate to nominal luminosity using the $\log L/L_\star \geq 5$ simulations.

Figure 10 repeats the same exercise in the stable envelope at $R = 33$ Mm. Based on the results of Herwig et al. (2023), we expect a $L^{2/3}$ scaling relation in this region where internal gravity wave (IGW) motions excited by the convective core characterize the

flow (we will demonstrate the IGW-dominated nature of the flow in Section 3.4). This is indeed what we recover for both setups at high luminosities, although there are important caveats to signal. First, there is a systematic offset between the 768^3 and 1152^3 scaling laws. This is the reflection of the fact that the velocities in the envelope are not yet converged with respect to the grid resolution (Section 3.2). Second, we see that in contrast with Figure 9 the $L^{2/3}$ scaling law holds down to smaller luminosities in the PM case than in the CPM case. Our interpretation is that the CPM case behaves just as expected, with the scaling law holding down to some small velocity beyond which the flow is not properly resolved. A priori, the PM simulations should show the same behaviour (i.e., a drop-off below the $L^{2/3}$ scaling law for $\log L/L_\star \leq 5$). However, as we have seen in Figure 9, the convective velocity spuriously increases at low heating rates, which necessarily result in stronger IGW motions in the envelope. This effect appears to compensate the expected IGW velocity drop-off at low luminosity. In other words, the fact that the $L^{2/3}$ scaling law holds well for all luminosities with the PM setup appears to be a coincidence resulting from the competition between two opposing effects.

3.4 Power spectra

We now go beyond spherical averages of the velocity field and investigate how much power the flow contains across different length scales. Figure 11 shows the power spectra of the rms velocity $|U|$ (top row) and radial velocity U_r (bottom row) at different radii in the star and for different Cartesian grid resolutions. The power is binned as a function of the angular degree ℓ . The maximum ℓ value shown in Figure 11 depends on the radius at which the power spectrum is calculated. A larger radius or grid resolution allows to capture smaller scale features, since the angular resolution of the projection of the Cartesian grid on a sphere increases. Note that the spectra are calculated using the filtered briquette data, which is down-sampled by a factor of 4 in each direction.

Both for $|U|$ and U_r , the power spectra in the convective core (blue lines, $R = 15$ Mm in Figure 11) display the expected Kolmogorov $\ell^{-5/3}$ cascade from large-scale modes ($\ell = 1 - 2$) down to very small scales ($\ell \sim 100$ for high-resolution runs) where dissipation takes place. The convective power spectra are consistently extended to higher ℓ values when the grid resolution is increased. This reflects the fact that the turbulent cascade extends down to the smallest spatial scales resolved in the simulation. In the stable envelope (green lines, $R = 35$ Mm) and in the semiconvective region (orange lines, $R = 25$ Mm), the U_r power spectra display a very different shape compared to the convective core, with a shallow increasing slope up to $\ell \sim 60$ followed by a rapid drop at higher ℓ . This shape is reminiscent of that found in the stable layers of our recent main-sequence and red giant branch PPMstar simulations (Herwig et al. 2023; Blouin et al. 2023b) and hints at the IGW-dominated nature of the flow at those radii. Contrarily to the convective power spectra, the power at all $\ell \lesssim 200$ continuously increases upon grid refinement. This behaviour is consistent with the previously noted absence of convergence for the velocities in the stable envelope of the CPM runs (Section 3.2). This increase in IGW power could conceivably be the result of the extension of the convective power spectra to larger ℓ values with increasing resolution. IGWs are possibly mainly excited by small-scale convective motions close to the core boundary, which would imply stronger IGW motions at high resolutions due to the enhanced power at high ℓ in the convective spectra.

For both setups, the 1152^3 and 1728^3 $|U|$ power spectra at $R = 35$ Mm is approaching convergence for $\ell \gtrsim 100$: the separation between the 1152^3 and 1728^3 spectra is smaller than that between the 768^3 and 1152^3 spectra. This is to be contrasted with the behaviour observed in the convective layers, where the power spectrum always extends to larger ℓ values upon grid refinement. This is most likely the result of radiative damping. Wave velocities are expected to be damped when radiative diffusion is taken into account, as the temperature of oscillating fluid parcels is equilibrated with their surroundings. This damping is stronger at large ℓ (Zahn et al. 1997), since small fluid parcels can lose their heat more quickly than large ones. This is consistent with the saturation of the IGW power spectrum observed in Figure 11. This result implies that radiative damping in our simulations only affects very small spatial scales ($\ell \gtrsim 100$) that require large Cartesian grids to be properly resolved (above 1152^3).

We have so far been discussing various properties of the IGWs in the stable envelope, but without explicitly demonstrating that IGWs indeed dominate fluid motions in that region of the star. We remediate this issue in Figure 12. We show power spectra taken at three different radii in run W20 (CPM setup, 1728^3 grid). Here, the power is binned both as a function of ℓ and the temporal frequency (the methodology used to calculate these spectra is detailed in Thompson et al. 2023).

The power spectra calculated in the convective core shows power spread out over a wide range of spatial and temporal frequencies with no clear structure, as expected for turbulent motions. In contrast, the power spectra calculated in the stable envelope (bottom panel) displays distinct ridges constituted of discrete modes. These discrete modes quickly disappear for frequencies that surpass the local Brunt–Väisälä frequency (represented here by a thin dotted line). This is precisely what is expected for IGWs, which are damped when the Brunt–Väisälä frequency is exceeded. Figure 13 further demonstrates the IGW nature of these modes. Here, we zoom in on the low- ℓ portion of the bottom panel of Figure 12 and overlay eigenmodes predictions from the stellar oscillation code GYRE (Townsend & Teitler 2013; Townsend et al. 2018). This analysis is performed as in Thompson et al. (2023) and is based on spherically averaged radial profiles from run W20. Two GYRE calculations were performed: one using the structure corresponding to the beginning of the series of dumps used in calculating the power spectrum from the simulation data and one using the last dump of that series. The frequencies shown in Figure 13 are the averages of these two calculations. The excellent agreement between the GYRE predictions definitely confirms that these modes are IGWs, and it even allows the identification of individual radial orders.

Going back to Figure 12, we now focus on the particularly interesting power spectrum of the semiconvection zone (middle panel). We see the same discrete ridges as in the stable envelope, signalling the presence of IGWs and indicating that the semiconvective layers are dominated by IGW motions. The power distribution is admittedly more smeared out than in the stable envelope where the ridges are well separated, but this is presumably due to shorter mode lifetimes. The lack of power at high ℓ and low frequencies is further indication of the absence of convective motions in this region. We will investigate the potential implications of the IGW-dominated nature of the semiconvection zone on CBM in Section 4.2.

4 ON THE NATURE OF THE CONVECTIVE BOUNDARY

Having described the main properties of the flow, established the numerical convergence properties of our simulations and obtained scaling relations, we now shift our focus to the CheB CBM problem introduced in Section 1. As a reminder, we have performed two series of simulations using two different initial setups with different CBM prescriptions because the accurate boundary mixing scheme is unknown. Can we use these simulations to infer the best CBM prescription to employ? In Section 4.1, we explore the most direct approach to tackle this question, namely investigating the evolution of the stratification in the boundary region.

4.1 Long-term evolution of the convective boundary

Figure 14 shows the time evolution of the μ profile in the boundary region for our $\log L/L_\star = 6$ simulations performed on a 1152^3 grid. For the CPM setup, we see that both the convective–semiconvective (left inset in the left panel) and semiconvective–radiative (right inset in the left panel) boundaries appear to be slowly migrating outward with time. The boundary is also changing for the PM setup, where the μ profile is steepening with the outer portion of the boundary moving inward (right inset in the right panel). These changes are admittedly small compared to the 0.07 Mm grid cell size of these simulations, but they nevertheless constitute a robust result that we recover at other grid resolutions and heating rates.

Note that these migrations do not show sign of slowing down

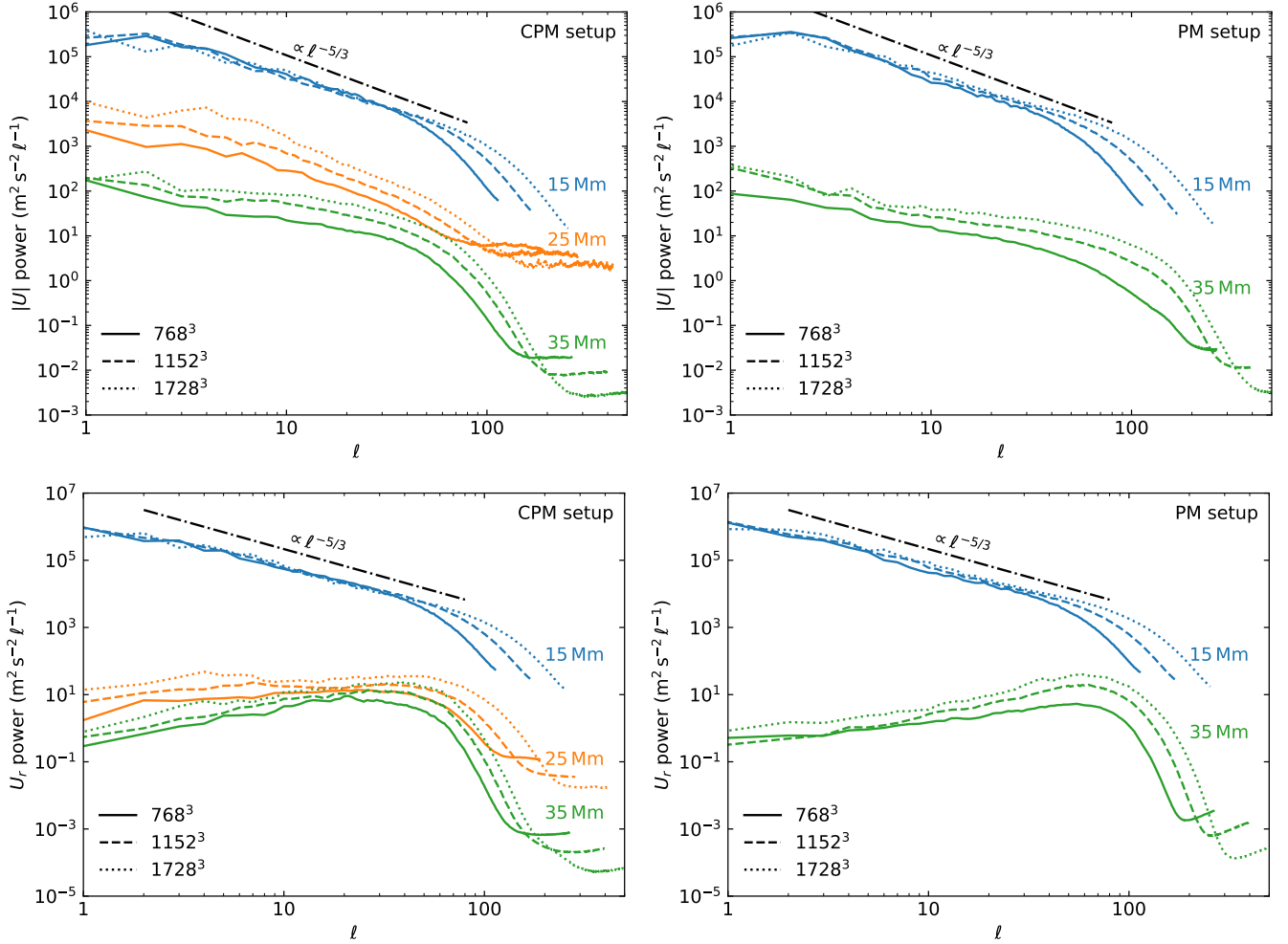


Figure 11. Power spectra of the rms velocity $|U|$ (top row) and radial velocity U_r (bottom row) taken at different radii in the simulations and for different grid resolutions. The spectra in blue are in the convective core, those in green are in the envelope, and for the CPM setup (left column) those in orange are in the semiconvective region. The spectra were calculated by averaging over dumps 800 to 1000 of our $\log L/L_\star = 5$ simulations (runs W12, W13, W20, W21, W22 and W23).

and approaching equilibrium after 40 h of simulation time. At the boundary, the radiative diffusivity is $D_{\text{rad}} \sim 10^{11} \text{ cm}^2 \text{ s}^{-1}$ in our $\log L/L_\star = 6$ simulations, which implies that heat diffusion had time to operate over a length scale of only $\sqrt{D_{\text{rad}} \cdot 40 \text{ h}} \sim 1 \text{ Mm}$. Hence, there is not enough time to reinstate thermal equilibrium following a local perturbation in the thermal structure of the stable layers due to a displacement of the convective boundary. It is therefore unsurprising that the boundary is still evolving at the end of our simulations, and reaching a stable boundary would demand much longer simulations (Anders et al. 2022a; Herwig et al. 2023; Mao et al. 2023). Nevertheless, it is tempting to extrapolate these trends to find the final equilibrated state towards which the simulations are evolving. For example, the apparent outward migration of the CPM setup may imply a larger mixed core than the one present in the initial MESA stratification.

However, such extrapolations are hazardous as it is not clear that these trends also apply to the real star. We have seen in Section 2.2 that the mapping between the MESA stratifications and the PPMstar base states is not perfect. The main problem is the omission of electron degeneracy pressure and ion-ion nonideal interactions in the equation of state currently employed by PPMstar, which leads to a

10% offset of the pressure profile. This inaccuracy affects the whole stratification, including the temperature and opacity profiles. This in turn perturbs the thermal balance of the star in a way that can be expected to shift its convective boundary. Another way to see this is to realize that a hypothetical MESA calculation with a different equation of state and/or opacity tables would yield a different convective boundary, since the Schwarzschild criterion would not be satisfied at the same radius. Hence, the small convective boundary reconfigurations observed in Figure 14 can at least partially be attributed to the response of the simulations to a change in the equation of state that has induced a state of thermal imbalance in the star. There is no obvious way to separate this behaviour from the (more interesting) 3D hydrodynamical response to the initial MESA base state, which is thermally balanced within the MLT framework.

All things considered, it is not currently possible to directly extrapolate the long-term evolution of our simulations to infer the “correct” stratification at the convective boundary of CHEB stars. Nevertheless, we will see in Sections 4.2 and 4.3 that we can gain further insights on the evolution of the convective boundary in our CPM simulations by isolating individual mixing processes through measurements of the diffusivity profile.

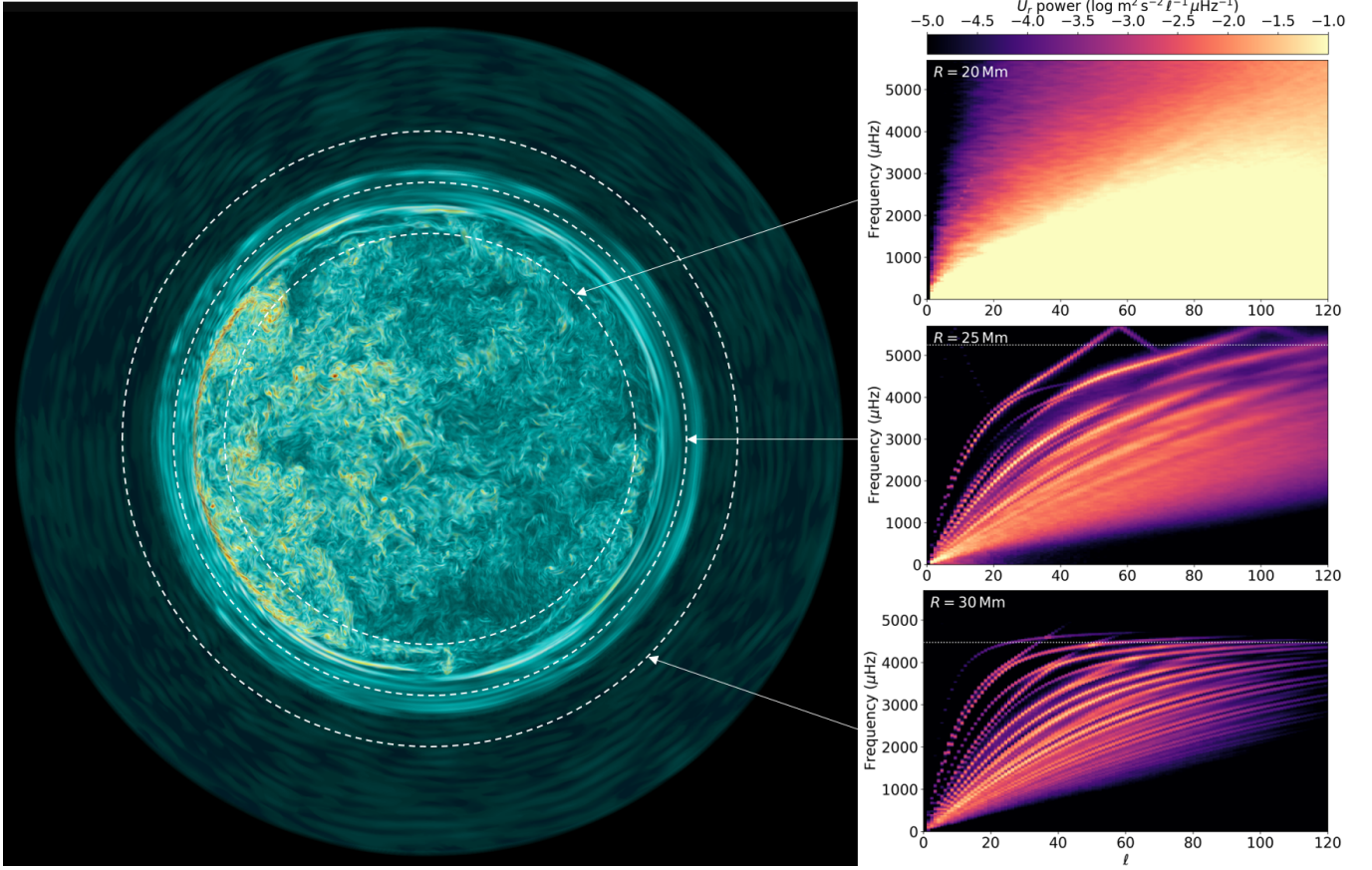


Figure 12. *Left:* Centre-plane slice rendering of the vorticity magnitude $|\nabla \times U|$ of run W20 (CPM setup, 1728^3 grid) at dump 840 ($t = 20.3$ h). Dark blue, turquoise, yellow, red, and dark red represent a sequence of increasing vorticity magnitudes. Unlike in Figure 6 and 7, the full simulation domain is shown. The white circles indicate the radii at which power spectra were calculated. *Right:* Power spectra of the radial velocity components at $R = 20, 25, 30$ Mm. The spectra were calculated over dumps 480 to 880 ($t = 11.6 - 21.3$ h). The local value of the Brunt-Väisälä frequency is shown by the dotted horizontal line.

4.2 IGW mixing

We have described in Section 3.4 how the semiconvection zone of our CPM simulations is dominated by strong IGW motions. Our recent simulations of core convection in massive main-sequence stars have revealed species mixing in stable layers with strong IGW motions, presumably because of IGW-induced mixing (Herwig et al. 2023). A priori, the same phenomenon could conceivably occur inside the semiconvection zones of CHEB stars. If it is the case, then this would provide a mechanism to homogenize and destroy the semiconvective interface.

We have measured the diffusion coefficient in our CPM simulations by inverting the observed evolution of the FV profile³ using the method described in Jones et al. (2017). The resulting diffusivity profile for a $\log L/L_\star = 6$ run is shown in black in Figure 15. Deep inside the convective core, the measured diffusivity is consistent with a simple MLT prescription (green dashed line). D becomes much smaller than the MLT value closer to the convective-semiconvective boundary, a well-known limitation of this simple prescription (Eggleton 1972; Jones et al. 2017; Herwig et al. 2023; Blouin et al. 2023a,b). Once we reach the semiconvection zone, D drops precipitously and

we cannot measure any mixing above $R = 23.7$ Mm. The mixing measured near the convective-semiconvective boundary is due to the overshooting motions that we will explore further in Section 4.3.

Beyond this boundary region, we measure no mixing in the semiconvection zone. This implies that despite their vigour, IGWs do not produce measurable mixing: we can establish an upper limit of $D_{\text{IGW}} \sim 10^9 \text{ cm}^2 \text{ s}^{-1}$ in the semiconvection of our $\log L/L_\star = 6$ simulations. Given the high heating rates of our simulations, we have every reason to believe that we are overestimating IGW mixing as we are overestimating IGW velocities by orders of magnitude. The upper limit on D_{IGW} implied by our simulations is therefore much smaller at nominal luminosity. In the absence of measurable IGW mixing in our simulations, it is of course impossible to establish a scaling relation for D_{IGW} that could be used to extrapolate to nominal luminosity. As an alternative, we can assume that the $D_{\text{IGW}} \propto L^{4/3}$ relation found in the IGW-dominated convective boundary layers of the H-core burning simulations without radiation diffusion of Herwig et al. (2023) still holds here. With this assumption, the upper limit on IGW mixing at nominal luminosity would be of only $\sim 10 \text{ cm}^2 \text{ s}^{-1}$. To evaluate whether this level of mixing could have an impact on the star, we estimate how long it would take to homogenize the semiconvective layers that are located above the radius where we can still measure D in Figure 15. It would take more than $(2 \text{ Mm})^2 / D_{\text{IGW}} \approx 130 \text{ Myr}$ to homogenize this 2 Mm-thick shell. This is a timescale comparable to

³ FV is the volume fraction that represents the contribution of the envelope fluid to the two-fluid mixture.

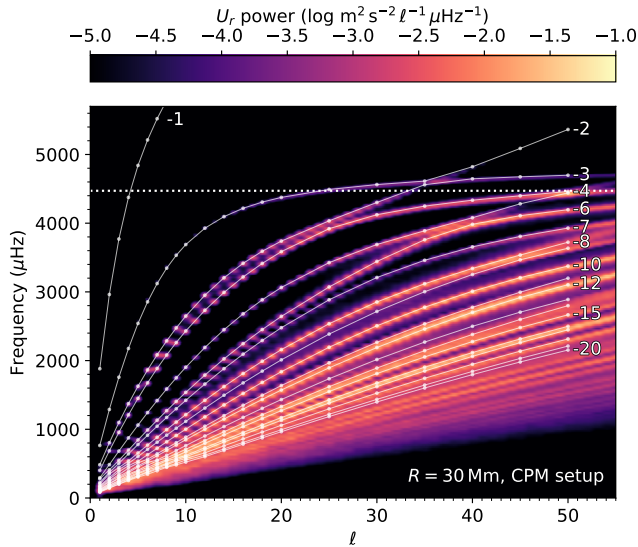


Figure 13. Power spectra of the radial velocity component at $R = 30$ Mm for run W20 calculated over dumps 480 to 880 ($t = 11.6 - 21.3$ h). The local value of the Brunt–Väisälä frequency is shown by the dotted horizontal line. The overlaid solid white lines show the eigenmodes predicted by GYRE for the stellar structure corresponding to that of run W20. The GYRE analysis was carried out using the spherically averaged structures of dumps 480 and 880: the frequencies shown here are averages of these two calculations. The labels next to the white lines indicate the radial orders n of the modes (their negative signs indicate that they are g modes).

the entire CHeB lifetime: IGW mixing in the semiconvection zone is negligible assuming the $D_{\text{IGW}} \propto L^{4/3}$ scaling relation is applicable to these simulations.

This result is consistent with the classical picture of semiconvection, where the diffusion coefficient in the semiconvective layers is taken to be (Langer et al. 1985)

$$D_{\text{sc}} = \alpha_{\text{sc}} \frac{K}{6c_P \rho} \frac{\nabla - \nabla_{\text{ad}}}{\nabla_L - \nabla}, \quad (5)$$

where α_{sc} is a free parameter that controls the mixing timescale, c_P is the heat capacity at constant pressure, and ∇_L is the Ledoux gradient. Once an adiabatic stratification is reached ($\nabla - \nabla_{\text{ad}} = 0$, as is the case in the semiconvective region of our CPM setup), no further mixing takes place and the composition profile remains constant if secular changes to the structure are neglected. In this picture, the amplitudes of IGWs saturate before they become strong enough to overturn (e.g., Merryfield 1995) and trigger nonlinear turbulent mixing.

4.3 Convective overshooting

We have seen in Figure 15 that, while no mixing is measured throughout most of the semiconvection zone, $D > 0$ in the layers close to the convective–semiconvective interface. This mixing is caused by strong convective motions that overshoot into the semiconvection zone. These overshooting motions are most clearly seen in our highest-heating runs, as exemplified by Figure 16. They gradually homogenize the semiconvection zone, thereby shrinking it to the benefit of the convective core. This is clearly shown in Figure 17. The black solid line shows the initial FV profile, and the coloured lines represent FV after 20 h of star time for 768³ simulations performed at different heating rates. The semiconvection zone is eroded to some

extent in all runs, but this is most striking for the highest-heating run (W32). Since all fluid motions are faster at higher heating, the evolution is effectively fast-forwarded and it is therefore natural to observe a faster erosion of the semiconvection zone.

There is also evidence that the morphology of the flow changes at high heating rates, with the development of larger overshooting motions. When the heating rate is increased, the convective motions are able to overshoot further into the semiconvection zone, a phenomenon clearly seen in the movies available at <https://www.ppmstar.org>. This phenomenon can also be detected in diffusivity profiles. Figure 18 shows the measured diffusivity profiles in our CPM simulations, calculated in each case in the $t = 20 - 25$ h interval. A first observation is that the agreement between simulations performed using different grid resolutions but identical heating rates is satisfactory. As we have seen in Figure 15, the radius at which D abruptly drops off marks the location of the convective–semiconvective interface. As the heating rate is increased, this point is pushed further outward in Figure 18 (≈ 22 Mm at $\log L/L_\star = 5$ compared to ≈ 23 Mm at $\log L/L_\star = 7$). This is a direct consequence of the faster evolution of the high-heating simulations. Past the convective boundary, Figure 18 reveals that the slope of the diffusivity profile is steeper at low heating rates. All other things being equal, this signals a faster damping of the overshooting motions at low heating rates, consistent with our observation that overshooting motions penetrate further into the semiconvection zone when the heating rate is increased.

Naturally, the astrophysically interesting question is to figure out whether these overshooting motions can homogenize the semiconvection zone at nominal heating. One way to attempt to answer this question is to establish a scaling relation for the core mass entrainment rate. Here, we define the entrained mass as being the total mass of envelope material located inward of $R = 22$ Mm. This definition is convenient as our PPMstar calculations follow the evolution of two fluids (a C/O-rich core fluid and an almost pure-He envelope fluid), but it will inevitably underestimate the true rate at which the convective core is eroding the semiconvective region in our simulations. Indeed, the semiconvective region is closer in composition to the convective core than to the stable envelope ($\text{FV} < 0.5$), meaning that most of the entrained mass is not captured by our definition. As we will see, this issue has no impact on the main conclusion of the mass entrainment rate analysis.

The top panel of Figure 19 demonstrates how the mass entrainment rate is measured for a given simulation, and the bottom panel shows the mass entrainment scaling relation thus found. To stay clear from the initial transient, we have evaluated the mass entrainment rates using only $t > 20$ h, and for more robust measurements we only employed simulations longer than 40 h. As in previous works (Jones et al. 2017; Androssy et al. 2020; Herwig et al. 2023; Mao et al. 2023), we find that the entrainment rate scales linearly with heating (if we exclude the lowest-heating run, consistent with our discussion in Section 3.3). Extrapolating this relation to nominal luminosity yields an entrainment rate of $4.5 \times 10^{-8} M_\odot \text{yr}^{-1}$. The 4 Mm-thick semiconvection zone contains $0.08 M_\odot$: at this rate it would take less than 2 Myr to completely erase it. This is much shorter than any relevant evolutionary timescale. In particular, it is significantly faster than the rate at which the convective core grows in CHeB stars (a growth rate of $\approx 3 \times 10^{-9} M_\odot \text{yr}^{-1}$ can be inferred from Figure 2). According to this analysis, we should therefore expect the semiconvection zone to be completely erased, implying that CHeB stars cannot have a semiconvection zone. Note that our restrictive definition of the entrained mass, which necessarily underestimates

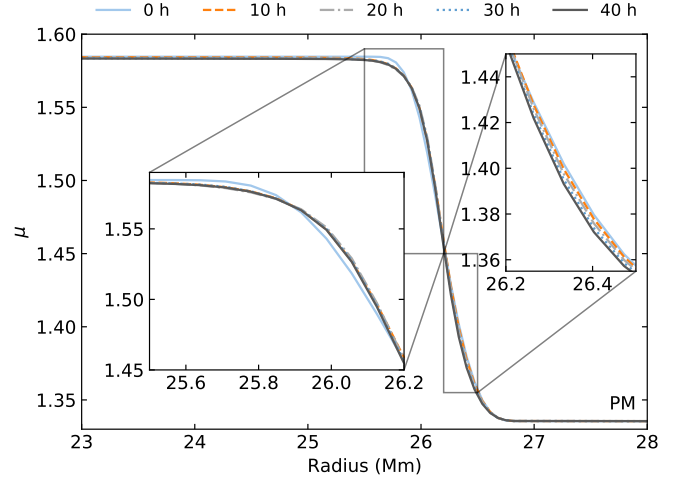
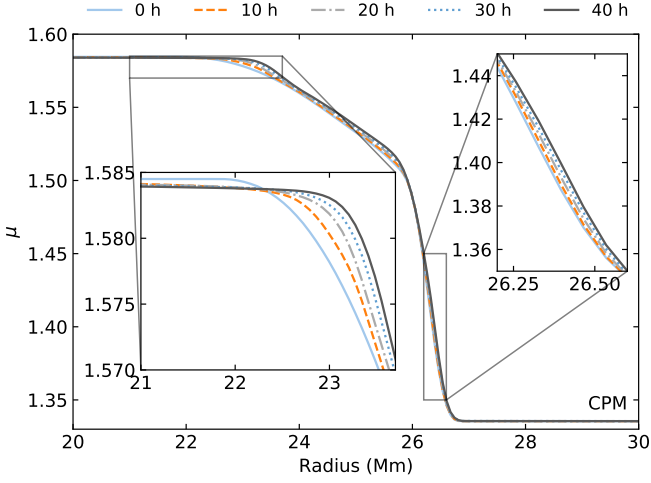


Figure 14. Evolution of the mean molecular weight profile in the boundary region for a CPM (left panel, run W28) and a PM (right panel, run W29) simulation. These runs employed a 1152^3 grid and a $\log L/L_\star = 6$ heating rate. The legends above the panels indicate the simulation times at which the profiles are shown.

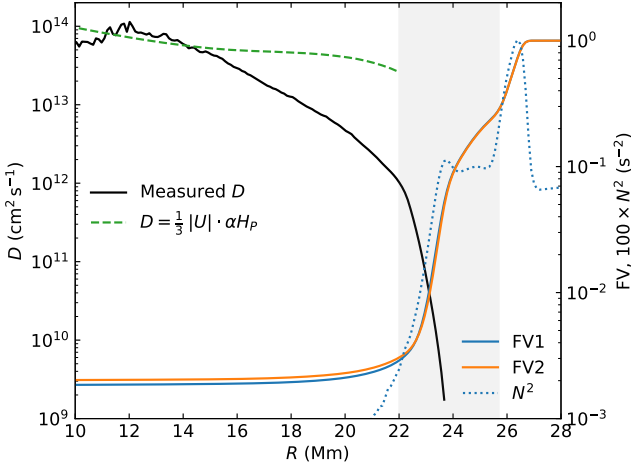


Figure 15. Measured diffusion coefficient (black solid line) in run W10 ($\log L/L_\star = 6$), where D was calculated by inverting the diffusion equation given the evolution of the FV profile between dumps 1300–1800 (blue solid line) and dumps 1800–2300 (orange solid line). No diffusion is measured above 23.7 Mm. The Brunt–Väisälä is given by the blue dotted line, and the grey region is the semiconvection zone. For comparison, the MLT diffusion coefficient $D = \frac{1}{3}|U|\alpha H_P$ is shown in green, where we have assumed that $\alpha = 0.25$ and that $|U|$ is given by the rms velocity profile in run W10.

the total entrained mass in our simulations, can only strengthen this conclusion.

However, there is a major caveat with this analysis. As explained in Section 4.1, the convective boundary may also be migrating for other spurious reasons related to the current PPMstar equation of state. When we measure an entrainment rate, we capture the sum of all the processes at play, and we may therefore be overestimating the rate at which the semiconvection zone is eroded due to real mixing processes. That being said, independent results also indicate that the semiconvection zone should be quickly erased. Anders et al. (2022b) have recently performed hydrodynamics simulations of an idealized plane-parallel setup containing a semiconvection zone between a convective and a stable region. They describe a similar be-

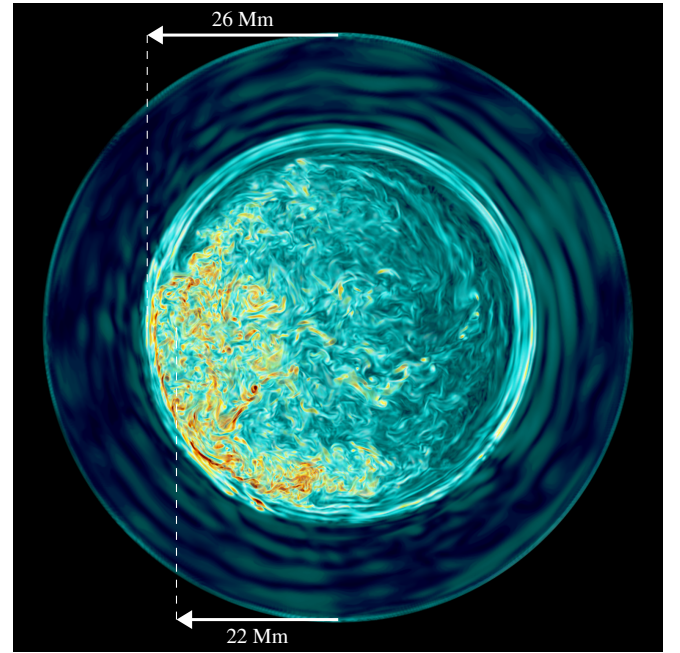


Figure 16. Center-plane slice rendering of the vorticity magnitude in run W32 (CPM setup, 768^3 grid, $\log L/L_\star = 7$) at dump 1650 ($t = 39.9$ h). In the southwest quadrant, note the intrusion of the dipole circulation pattern of the convective core into the semiconvective layers. This is to be contrasted with the $\log L/L_\star = 5$ simulation rendered in Figures 6 and 12, where the turbulent motions are confined to a spherical region circumscribed by a clear boundary at $R \approx 22$ Mm.

haviour to that detailed above, with overshooting convective motions gradually entraining low- μ material into the convective region and homogenizing the semiconvective layers. Ultimately, after thousands of convective turnover timescales, they report the disappearance of the semiconvection zone.

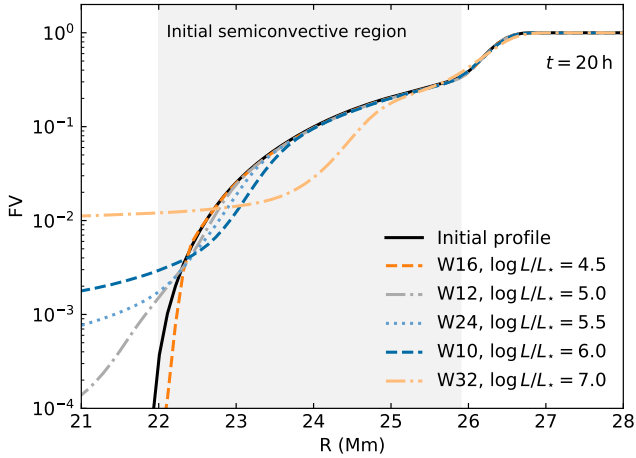


Figure 17. FV profile at $t = 20$ h for our CPM runs performed on a 768^3 Cartesian grid and with different heating rates (see legend). The black solid line corresponds to the initial setup. The semiconvection zone in the initial setup is shaded in grey. Note how the FV profile in the semiconvective layers is homogenized in the highest-heating run (W32).

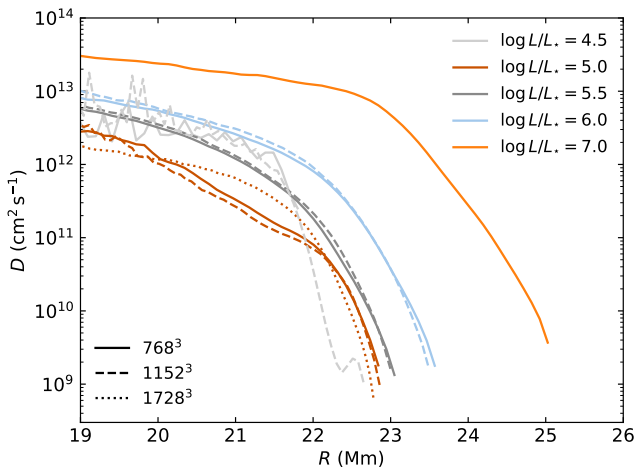


Figure 18. Measured diffusion coefficient in our CPM simulations (see legend for grid resolution and heating rate). For each run, D was calculated by inverting the evolution of the FV profile between $t = 20.0 - 22.5$ h and $t = 22.5 - 25.0$ h.

5 CONCLUSION

We have presented the first full-sphere 3D hydrodynamics simulations of the interior of a CHeB star. For dozens of convective turnover timescales, we followed the hydrodynamical response of our high-resolution simulations to two different initial stratifications (one with a semiconvective region and one without) for a $3 M_{\odot}$ CHeB star.

We have recovered many of the key findings of our recent simulations of core convection in massive main-sequence stars, including the presence of a large dipole circulation pattern in the convective core, the excitation of a rich spectrum of IGWs in the stable envelope consistent with the eigenfrequencies predicted by GYRE for the same stratification, and the $L^{1/3}$ and $L^{2/3}$ scaling of the convective and IGW velocities, respectively. We found that the extended core of the PM prescription remains fully convective even if $\nabla_{\text{rad}} - \nabla_{\text{ad}}$ becomes

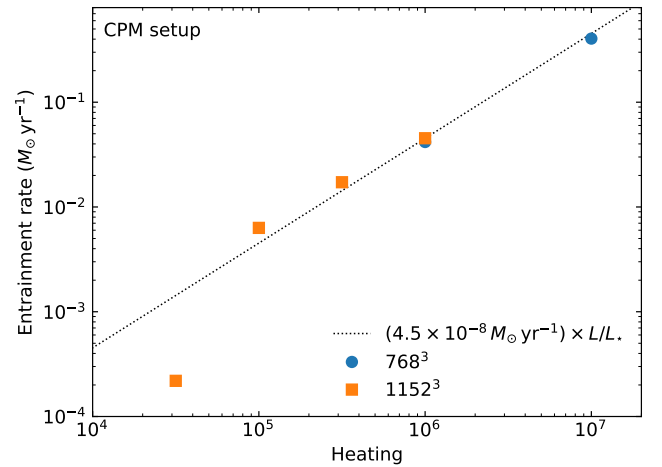
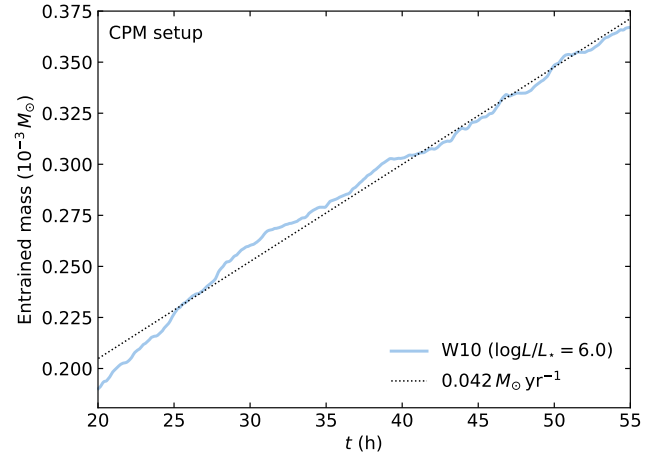


Figure 19. *Top:* Time evolution of the entrained mass in run W10 (blue line, $\log L/L_{\star} = 6$ and 768^3 grid) and best-fit linear entrainment rate (black dotted line). *Bottom:* Heating series of the measured mass entrainment rate (blue and orange symbols) and best-fit linear scaling law (black dotted line). The $\log L/L_{\star} = 4.5$ run was omitted from the fit.

very close to 0 (while remaining positive). We have described how an hypothetical semiconvection zone would be dominated by IGW motions. Despite the high amplitudes of these waves, we see no evidence for IGW mixing, in contrast with our recent finding for the core boundary region of massive main-sequence stars (Herwig et al. 2023).

For simulations initialized with a semiconvective interface, we have also observed the incursion of convective motions inside the semiconvective zone, a phenomenon that gradually erases this region. While the efficiency of this mixing process at nominal luminosity remains unclear, it could be sufficient to homogenize the semiconvection zone of a CHeB star much more rapidly than any relevant evolutionary timescale. This would imply, as recently suggested by Anders et al. (2022b), that CHeB stars cannot harbour a semiconvective interface between their C/O-rich cores and He envelopes.

Future research should investigate other CBM prescriptions beyond the MESA CPM and PM schemes to model the CHeB phase. A growing body of work (Anders et al. 2022a; Androssy et al. 2023; Baraffe et al. 2023; Blouin et al. 2023b; Mao et al. 2023) is suggesting that the stratifications implied by these two CBM schemes is not

appropriate. In particular, multi-dimensional hydrodynamics simulations consistently point to the formation of a convective penetration zone where the temperature gradient smoothly transitions from ∇_{ad} to ∇_{rad} over a fraction of a pressure scale height ($\sim 0.1 - 1 H_P$). This is in clear tension with the discontinuous transitions implied by MESA's CPM and PM schemes.

ACKNOWLEDGEMENTS

SB is a Banting Postdoctoral Fellow and a CITA National Fellow, supported by the Natural Sciences and Engineering Research Council of Canada (NSERC). FH acknowledges funding through an NSERC Discovery Grant. PRW acknowledges funding through NSF grants 1814181 and 2032010. FH and PRW have been supported through NSF award PHY-1430152 (JINA Center for the Evolution of the Elements). The simulations presented in this work were carried out on the NSF Frontera supercomputer operated by the Texas Advanced Computing Center at the University of Texas at Austin and on the Compute Canada Niagara supercomputer operated by SciNet at the University of Toronto. The data analysis was carried on the Astrohub online virtual research environment (<https://astrohub.uvic.ca>) developed and operated by the Computational Stellar Astrophysics group (<http://csa.phys.uvic.ca>) at the University of Victoria and hosted on the Compute Canada Arbutus Cloud at the University of Victoria.

DATA AVAILABILITY

Simulation outputs are available at <https://www.ppmstar.org> along with the Python notebooks that have been used to generate the figures presented in this work.

REFERENCES

- Althaus L. G., García-Berro E., Isern J., Córscico A. H., Miller Bertolami M. M., 2012, *A&A*, **537**, A33
- Anders E. H., Jermyn A. S., Lecoanet D., Brown B. P., 2022a, *ApJ*, **926**, 169
- Anders E. H., Jermyn A. S., Lecoanet D., Fraser A. E., Cresswell I. G., Joyce M., Fuentes J. R., 2022b, *ApJ*, **928**, L10
- Andrassy R., Herwig F., Woodward P., Ritter C., 2020, *MNRAS*, **491**, 972
- Andrassy R., Leidi G., Higl J., Edelmann P. V. F., Schneider F. R. N., Roepke F. K., 2023, *arXiv e-prints*, p. [arXiv:2307.04068](https://arxiv.org/abs/2307.04068)
- Asplund M., Grevesse N., Sauval A. J., Scott P., 2009, *ARA&A*, **47**, 481
- Baraffe I., Pratt J., Vlaykov D. G., Guillet T., Goffrey T., Le Saux A., Constantino T., 2021, *A&A*, **654**, A126
- Baraffe I., et al., 2023, *MNRAS*, **519**, 5333
- Bauer E. B., 2023, *ApJ*, **950**, 115
- Bédard A., Bergeron P., Brassard P., Fontaine G., 2020, *ApJ*, **901**, 93
- Biermann L., 1932, *Z. Astrophys.*, **5**, 117
- Blouin S., Daligault J., Saumon D., Bédard A., Brassard P., 2020, *A&A*, **640**, L11
- Blouin S., Daligault J., Saumon D., 2021, *ApJ*, **911**, L5
- Blouin S., Mao H., Woods T. E., Denissenkov P., Woodward P. R., Herwig F., 2023a, *MNRAS*, **521**, 4605
- Blouin S., Mao H., Herwig F., Denissenkov P., Woodward P. R., Thompson W. R., 2023b, *MNRAS*, **522**, 1706
- Bossini D., et al., 2015, *MNRAS*, **453**, 2290
- Boylan-Kolchin M., Weisz D. R., 2021, *MNRAS*, **505**, 2764
- Caputo F., Castellani V., Chieffi A., Pulone L., Tornambe A. J., 1989, *ApJ*, **340**, 241
- Cassisi S., Castellani V., Degl'Innocenti S., Piotto G., Salaris M., 2001, *A&A*, **366**, 578
- Cassisi S., Salaris M., Irwin A. W., 2003, *ApJ*, **588**, 862
- Castellani V., Giannone P., Renzini A., 1971a, *Ap&SS*, **10**, 340
- Castellani V., Giannone P., Renzini A., 1971b, *Ap&SS*, **10**, 355
- Castellani V., Chieffi A., Tornambe A., Pulone L., 1985, *ApJ*, **296**, 204
- Charpinet S., et al., 2011, *A&A*, **530**, A3
- Charpinet S., Brassard P., Giammichele N., Fontaine G., 2019a, *A&A*, **628**, L2
- Charpinet S., et al., 2019b, *A&A*, **632**, A90
- Chidester M. T., Timmes F. X., Farag E., 2023, *arXiv e-prints*, p. [arXiv:2307.03965](https://arxiv.org/abs/2307.03965)
- Cimatti A., Moresco M., 2023, *arXiv e-prints*, p. [arXiv:2302.07899](https://arxiv.org/abs/2302.07899)
- Constantino T., Campbell S. W., Christensen-Dalsgaard J., Lattanzio J. C., Stello D., 2015, *MNRAS*, **452**, 123
- Constantino T., Campbell S. W., Lattanzio J. C., van Duijneveldt A., 2016, *MNRAS*, **456**, 3866
- Constantino T., Campbell S. W., Lattanzio J. C., 2017, *MNRAS*, **472**, 4900
- De Gerónimo F. C., Battich T., Miller Bertolami M. M., Althaus L. G., Córscico A. H., 2019, *A&A*, **630**, A100
- Denissenkov P. A., VandenBerg D. A., Kopacki G., Ferguson J. W., 2017, *ApJ*, **849**, 159
- Dorman B., Rood R. T., 1993, *ApJ*, **409**, 387
- Eggleton P. P., 1972, *MNRAS*, **156**, 361
- Fantini N. J., et al., 2019, *ApJ*, **887**, 148
- Fontaine G., Brassard P., Bergeron P., 2001, *PASP*, **113**, 409
- Gabriel M., Noels A., Montalbán J., Miglio A., 2014, *A&A*, **569**, A63
- Giammichele N., et al., 2018, *Nature*, **554**, 73
- Giammichele N., Charpinet S., Brassard P., 2022, *Frontiers in Astronomy and Space Sciences*, **9**, 879045
- Hansen B. M. S., et al., 2013, *Nature*, **500**, 51
- Herwig F., et al., 2023, *arXiv e-prints*, p. [arXiv:2303.05495](https://arxiv.org/abs/2303.05495)
- Iglesias C. A., Rogers F. J., 1996, *ApJ*, **464**, 943
- Jones S., Andrassy R., Sandalski S., Davis A., Woodward P., Herwig F., 2017, *MNRAS*, **465**, 2991
- Kaiser B. C., Clemens J. C., Blouin S., Dufour P., Hegedus R. J., Reding J. S., Bédard A., 2021, *Science*, **371**, 168
- Käpylä P. J., 2019, *A&A*, **631**, A122
- Langer N., El Eid M. F., Fricke K. J., 1985, *A&A*, **145**, 179
- Li Y., Chen X.-h., Xiong H.-r., Guo J.-j., Chen X.-f., Han Z.-w., 2018, *ApJ*, **863**, 12
- Mao H., Woodward P., Herwig F., Denissenkov P. A., Blouin S., Thompson W., 2023, *arXiv e-prints*, p. [arXiv:2304.10470](https://arxiv.org/abs/2304.10470)
- Merryfield W. J., 1995, *ApJ*, **444**, 318
- Michaud G., Richer J., Richard O., 2007, *ApJ*, **670**, 1178
- Montalbán J., Miglio A., Noels A., Dupret M. A., Scuflaire R., Ventura P., 2013, *ApJ*, **766**, 118
- Montgomery M. H., Klumpe E. W., Winget D. E., Wood M. A., 1999, *ApJ*, **525**, 482
- Müller B., Viallet M., Heger A., Janka H.-T., 2016, *ApJ*, **833**, 124
- Ostrowski J., Baran A. S., Sanjayan S., Sahoo S. K., 2021, *MNRAS*, **503**, 4646
- Paczynski B., 1970, *Acta Astron.*, **20**, 195
- Paxton B., Bildsten L., Dotter A., Herwig F., Lesaffre P., Timmes F., 2011, *ApJS*, **192**, 3
- Paxton B., et al., 2013, *ApJS*, **208**, 4
- Paxton B., et al., 2015, *ApJS*, **220**, 15
- Paxton B., et al., 2018, *ApJS*, **234**, 34
- Paxton B., et al., 2019, *ApJS*, **243**, 10
- Porter D. H., Woodward P. R., 2000, *ApJS*, **127**, 159
- Renedo I., Althaus L. G., Miller Bertolami M. M., Romero A. D., Córscico A. H., Rohmann R. D., García-Berro E., 2010, *ApJ*, **717**, 183
- Salaris M., Cassisi S., 2017, *Royal Society Open Science*, **4**, 170192
- Salaris M., Domínguez I., García-Berro E., Hernanz M., Isern J., Mochkovitch R., 1997, *ApJ*, **486**, 413
- Salaris M., García-Berro E., Hernanz M., Isern J., Saumon D., 2000, *ApJ*, **544**, 1036
- Salaris M., Cassisi S., Pietrinferni A., Kowalski P. M., Isern J., 2010, *ApJ*, **716**, 1241
- Salaris M., Cassisi S., Pietrinferni A., Hidalgo S., 2022, *MNRAS*, **509**, 5197

Schwarzschild M., Härm R., 1969, *BAAS*, 1, 99
 Segretain L., Chabrier G., Hernanz M., Garcia-Berro E., Isern J., Mochkovitch R., 1994, *ApJ*, 434, 641
 Spruit H. C., 2015, *A&A*, 582, L2
 Stephens D., Herwig F., Woodward P., Denissenkov P., Androssy R., Mao H., 2021, *MNRAS*, 504, 744
 Straniero O., Domínguez I., Imbriani G., Piersanti L., 2003, *ApJ*, 583, 878
 Sweigart A. V., Demarque P., 1973, in Fernie J. D., ed., *Astrophysics and Space Science Library Vol. 36*, IAU Colloq. 21: Variable Stars in Globular Clusters and in Related Systems. p. 221, doi:10.1007/978-94-010-2590-4_32
 Thompson W., Herwig F., Woodward P. R., Mao H., Denissenkov P., Bowman D. M., Blouin S., 2023, *arXiv e-prints*, p. arXiv:2303.06125
 Townsend R. H. D., Teitler S. A., 2013, *MNRAS*, 435, 3406
 Townsend R. H. D., Goldstein J., Zweibel E. G., 2018, *MNRAS*, 475, 879
 Uzundag M., et al., 2021, *A&A*, 651, A121
 Van Grootel V., Charpinet S., Fontaine G., Green E. M., Brassard P., 2010a, *A&A*, 524, A63
 Van Grootel V., et al., 2010b, *ApJ*, 718, L97
 Woodward P. R., Herwig F., Lin P.-H., 2015, *ApJ*, 798, 49
 Woodward P. R., Herwig F., Wetherbee T., 2018, *Computing in Science and Engineering*, 20, 8
 Woodward P. R., Lin P.-H., Mao H., Androssy R., Herwig F., 2019, in *Journal of Physics Conference Series*. p. 012020 (arXiv:1810.13416), doi:10.1088/1742-6596/1225/1/012020
 Zahn J. P., Talon S., Matias J., 1997, *A&A*, 322, 320

Table A1. Opacity model fit parameters

$\log R_1$	-2.37164275	$\log R_2$	-1.77937633
$X_{\text{CO},1}$	0.00000000	$X_{\text{CO},2}$	0.73187004
a_{11}^0	0.29340722	a_{12}^0	-0.59945332
a_{11}^1	-1.02164622	a_{12}^1	2.72183141
a_{11}^2	1.13886313	a_{12}^2	-5.12118290
a_{11}^3	-0.27116766	a_{12}^3	5.12686032
a_{11}^4	-0.39983029	a_{12}^4	-2.99192563
a_{11}^5	0.44397946	a_{12}^5	1.08999269
a_{21}^0	0.30510341	a_{22}^0	-0.51150380
a_{21}^1	-1.01849526	a_{22}^1	2.94414203
a_{21}^2	0.97161241	a_{22}^2	-7.04134649
a_{21}^3	0.13445119	a_{22}^3	8.72264878
a_{21}^4	-0.88449144	a_{22}^4	-5.95817987
a_{21}^5	0.69582918	a_{22}^5	2.15246120

APPENDIX A: OPACITY MODEL

The polynomial opacity model used in our PPMstar simulations has the form

$$\kappa = \sum_{i=0}^5 b_i (T_7)^{5-i}, \quad (\text{A1})$$

where $T_7 = \log T - 7$. The b_i coefficients are obtained via bilinear interpolation in the mass fraction and $\log R \equiv \log \rho - 3 \log T + 18$ space,

$$b_i = w_{11} a_{11}^i + w_{12} a_{12}^i + w_{21} a_{21}^i + w_{22} a_{22}^i. \quad (\text{A2})$$

The a_{jk}^i fit parameters are given in Table A1, and the bilinear interpolation weights w_{jk} are given by

$$\begin{aligned} w_{11} &= (\log R_2 - \log R)(X_{\text{CO},2} - X_{\text{CO}})/\alpha, \\ w_{12} &= (\log R_2 - \log R)(X_{\text{CO}} - X_{\text{CO},1})/\alpha, \\ w_{21} &= (\log R - \log R_1)(X_{\text{CO},2} - X_{\text{CO}})/\alpha, \\ w_{22} &= (\log R - \log R_1)(X_{\text{CO}} - X_{\text{CO},1})/\alpha, \end{aligned} \quad (\text{A3})$$

with

$$\alpha = (\log R_2 - \log R_1)(X_{\text{CO},2} - X_{\text{CO},1}). \quad (\text{A4})$$

X_{CO} is the combined mass fraction of C and O. We stress that this opacity model is reliable only within the limited composition–temperature–density space covered by our simulations.

This paper has been typeset from a $\text{\TeX}/\text{\LaTeX}$ file prepared by the author.